A Moving Morphable Components Based Shape Reconstruction Framework for Electrical Impedance Tomography

Dong Liu and Jiangfeng Du

***Abstract*— This paper presents a new computational framework in electrical impedance tomography (EIT) for shape reconstruction based on the concept of moving morphable components (MMC). In the proposed framework, the shape reconstruction problem is solved in an explicit and geometrical way. Compared with the traditional pixel or shape-based solution framework, the proposed framework can incorporate more geometry and prior information into shape and topology optimization directly and therefore render the solution process more flexibility. It also has the afford potential to substantially reduce the computational burden associated with shape and topology optimization. The effectiveness of the proposed approach is tested with noisy synthetic data and experimental data, which demonstrates the most popular biomedical application of EIT: lung imaging. In addition, robustness studies of the proposed approach considering modeling errors caused by non-homogeneous background, varying initial guesses, differing numbers of candidate shape components, and differing exponent in the shape and topology description function are performed. The simulation and experimental results show that the proposed approach is tolerant to modeling errors and is fairly robust to these parameter choices, offering significant improvements in image quality in comparison to the conventional absolute reconstructions using smoothness prior regularization and total variation regularization.**

***Index Terms*— Electrical impedance tomography, shape optimization, topology optimization, moving morphable component, lung imaging, inverse problems.**

Manuscript received April 29, 2019; accepted May 20, 2019. Date of publication May 23, 2019; date of current version November 26, 2019. This work was supported in part by the National Natural Science Foundation of China under Grant 81788101, Grant 61871356, and Grant 11761131011, in part by the National Key R&D Program of China under Grant 2018YFA0306600, in part by the Chinese Academy of Sciences under Grant GJJSTD20170001 and Grant QYZDY-SSW-SLH004, and in part by the Anhui Initiative in Quantum Information Technologies under Grant AHY050000, and in part by the Anhui Provincial Natural Science Foundation under Grant 1708085MA25. *(Corresponding authors: Dong Liu; Jiangfeng Du.)*

The authors are with Hefei National Laboratory for Physical Sciences, Microscale and Department of Modern Physics, University of Science and Technology of China, Hefei 230026, China, also with the CAS Key Laboratory of Microscale Magnetic Resonance, University of Science and Technology of China, Hefei 230026, China, and also with the Synergetic Innovation Center of Quantum Information and Quantum Physics, University of Science and Technology of China, Hefei 230026, China (e-mail: dong.liu@outlook.com; djf@ustc.edu.cn).

Color versions of one or more of the figures in this article are available online at http://ieeexplore.ieee.org.

Digital Object Identifier 10.1109/TMI.2019.2918566

I. Introduction

ELECTRICAL impedance tomography (EIT) is an imaging modality that aims to reconstruct the impedance distribution inside an object of interest from electrical measurement on the body surface. Because of its non-invasiveness, portability and practical utilities, EIT has been considered in a number of medical [1]–[4] and industrial applications [5]–[7], leading to many useful and promising results across a spectrum of fields.

The EIT image reconstruction problem is a nonlinear ill-posed inverse problem. Utilizing prior information is critical in addressing the EIT reconstruction problem (see, e.g., [8]–[13] for a partial list). To solve such a challenging problem, regularization is needed to overcome the extreme sensitivity to measurement noise and modeling errors [14]–[19].

The idea of accounting for shape information based regularization in the reconstruction is gaining increasing interest within the scientific community. Several recent studies [20]–[28] in both medical and industrial applications have explored applying prior shape information with the objective of improving image quality. Shape-based reconstruction methods have been employed with wide success to determine information concerning the size, shape, location and perhaps the number of anomalies across multiple application realms arising in medical imaging and industrial field. Despite this success, a withstanding challenge in shape reconstruction is the ability to impose the prior shape information in an explicit and geometrical way. For example, the factorization method, that was motivated from the inverse scattering problem [29], is useful for recovering the shape information, e.g., conductivity change in EIT [20], [30]; however, its effectiveness may be questionable in cases using a small amount of data and it is not presently clear how to incorporate systematic a priori information concerning either the geometric/topological (e.g., number of conductivity components) or physical properties of the conductivity which is necessary for the method to work. Concerning other direct shape reconstruction methods, see the monotonicity-based regularization method [31]–[33], the enclosure method [34], [35] and the D-bar method [4], [15], [36] for a partial list.

From a geometry representation point of view, most of the existing reconstruction methods are developed within the

shape-based solution framework. For example, in the well-established level set approaches [37], [38], a shape and topology description function (STDF), also called a level set function (LSF), is used to implicitly represent the boundary of the targets as the zero level set (with respect to the space variables) with one higher dimension, and it easily handles topological changes. In traditional level set (TLS) methods, during the reconstruction, the shape boundary evolution is described by a Hamilton-Jacobi partial differential equation (PDE) and is driven by the extension velocity field derived from shape sensitivity analysis. Although significant progress has been in the field of shape reconstruction using TLS methods, there still exist some challenging issues which need to be further addressed [39]. One of them is that when applying TLS for shape reconstruction, the implementation of the conventional discrete level set methods requires appropriate choice of the upwind schemes, reinitialization algorithms and extension velocity methods, which may limit the application of the TLS to EIT shape reconstruction problems.

To overcome these aforementioned drawbacks and retain the topological benefits of the implicit representation of evolving boundary, the parametric level set (PLS) methods have been extensively carried out within the scientific community, such as structural topology optimization [40], [41], seismic imaging and inversion [42], EIT [23], [26], [43], etc. The key idea of PLS is to represent the implicit STDF in a parametric way, i.e., expressing the STDF parametrically as a linear combination of a predefined radial basis functions (RBFs) and (unknown) weighting parameters, thus the Hamilton-Jacobi PDE will be transformed into a series of ordinary differential equations through the parameterization process [44]. PLS parameterization waives reinitialization of the STDF unlike in traditional LSM, and thus makes the method more efficient to implement and also improves the condition number of the inverse problem as compared to TLS methods. However, with a RBF function, the corresponding weights have no physical meaning and their ranges cannot be determined explicitly. In practice, these bounds can only be empirically set. Furthermore, another problem that has not been fully addressed yet is the determination of the initial distribution of RBF centers.

In the present work, with the primary aim of conducting shape reconstruction in a more geometrically explicit and flexible way, a so-called moving morphable components (MMC) based shape reconstruction framework is proposed. The idea of MMC was originally introduced by Guo *et al.* [45] for structure topology optimization, and it was subsequently extensively carried out by Guo's team in [46]–[54]. The key idea of this MMC-based reconstruction approach is that a set of morphable components represented by STDFs with variable parameters (such as lengths, thicknesses, orientations) are used as the basic blocks of shape reconstruction (see Fig. 1 for a schematic illustration). The optimal shape, i.e., conductivity distribution, is found by optimizing STDF parameters (lengths, thicknesses, orientations) and layout (connectivity) of these morphable components. Compared with the level set-based solution framework, the proposed MMC-based framework has the following distinctive features: ① The shape of the components is described by using explicit STDF so that it is able to incorporate more geometric information into shape reconstruction directly and therefore render the solution process more flexibility; ② The proposed framework has significant potential to improve the conditional number of the reconstruction problem and also reduce the computational demand associated with shape reconstruction. In the proposed framework, shape description parameters of the components are adopted as unknown variables. As a consequence, the number of unknown variables may be quite smaller than that involved in traditional STDF-based approaches. ③ The proposed framework offers a mechanism to effectively incorporate the priori information, such as position, size, etc, of the target object to be imaged into the reconstruction problem, ④ It can be easily extended to three-dimensional applications. Table I gives a comparison of the STDF construction, geometry representation and dimension reduction properties associated with level set based shape reconstruction approaches and the proposed approach.

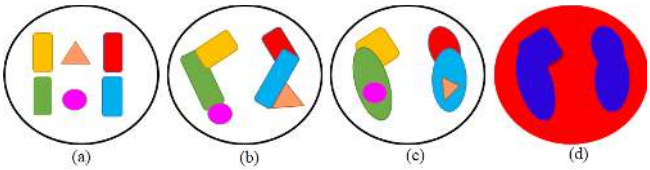

Fig. 1. Moving morphable components as basic blocks of shape reconstruction. (a): Simple candidate components. (b)&(c): Complex shape topologies. (d): An example of conductivity distribution based on the MMCs in (c), by assigning binary conductivity to the components and background, respectively.

Finally, we evaluate the performance of the proposed MMC-based reconstruction method via simulations and phantom studies. Both numerical and experimental studies demonstrate the most popular biomedical application of EIT: lung imaging. In addition, robustness studies of the proposed approach considering modeling errors caused by non-homogeneous background (e.g., simulated aorta and heart are presented in the measurement domain), differing numbers of candidate shape components, and differing exponent in the STDF are performed. The simulation and experimental results show that the proposed approach tolerates these kinds of modeling errors well and is fairly robust to these parameter choices, leading to high-quality shape reconstructions, as measured by quantitative metrics such as structural similarity (SSIM) index, relative inclusion area coverage ratio and relative contrast for the binary conductivity. The results are compared against the conventional absolute reconstructions using smoothness prior regularization and total variation regularization.

The remainder of this paper is structured as follows: we briefly review the EIT forward model in Section II. The properties of the proposed MMC-based framework are discussed in Section III. In Section IV, we overview the EIT simulations, experimental setup, test cases as well as the implementation details. The numerical and experimental results are presented in Section V, and some concluding remarks are given in the last section.

II. EIT Forward Problem

In EIT, to perform bioimpedance measurements, an electrode belt containing L electrodes is placed around the

TABLE I
A COMPARISON OF DIFFERENT STDF-BASED RECONSTRUCTION APPROACHES

Method	STDF construction	Geometry representation	Dimension reduction
Traditional level set	Implicit	Implicit	No
Parametric level set	Explicit	Implicit	Yes
MMC-based approach	Explicit	Explicit	Yes

body surface. Let us denote the body under investigation by $\Omega \subset \mathbb{R}^q, q = 2, 3$, and its boundary by $\partial\Omega$. A set of electric currents is injected into the body through these electrodes, and the corresponding voltages are measured using the same electrodes. The forward problem of EIT can be stated as follows: given a conductivity distribution $\sigma(\boldsymbol{x})$ within Ω and a current injection pattern I_ℓ, compute the electrical voltage $U(\boldsymbol{x})$ on the measurement boundary $\partial\Omega$. In this work, the dependence of $\sigma(\boldsymbol{x})$ on electrode measurements is modeled by the Complete Electrode Model (CEM) [55], which consists of the Laplace equation

$$\nabla \cdot (\sigma(\boldsymbol{x})\nabla u(\boldsymbol{x})) = 0, \quad \boldsymbol{x} \in \Omega, \tag{1}$$

and the boundary conditions

$$u(\boldsymbol{x}) + z_\ell \sigma(\boldsymbol{x}) \frac{\partial u(\boldsymbol{x})}{\partial \nu} = U_\ell, \quad \boldsymbol{x} \in e_\ell, \ \ell = 1, ..., L, \tag{2}$$

$$\int_{e_\ell} \sigma(\boldsymbol{x}) \frac{\partial u(\boldsymbol{x})}{\partial \nu} \mathrm{d}S = I_\ell, \quad \ell = 1, ..., L, \tag{3}$$

$$\sigma(\boldsymbol{x}) \frac{\partial u(\boldsymbol{x})}{\partial \nu} = 0, \quad \boldsymbol{x} \in \partial\Omega \backslash \bigcup_{\ell=1}^{L} e_\ell, \tag{4}$$

where $\boldsymbol{x} \in \Omega$ is the spatial coordinate, z_ℓ is the contact impedance between electrodes and the imaged body; U_ℓ denotes the potential corresponding to electrode e_ℓ; ν denotes an outward unit normal.

In addition, the electric current must satisfy the charge conservation law

$$\sum_{\ell=1}^{L} I_\ell = 0. \tag{5}$$

To determine uniquely the potentials $u(\boldsymbol{x})$ and U_ℓ based on the CEM, the reference potential must be fixed, for instance, by setting

$$\sum_{\ell=1}^{L} U_\ell = 0. \tag{6}$$

Approximating the CEM model (1-6) with finite element method (FEM) and assuming an additive noise model leads to the observation model:

$$V = U(\sigma) + e, \tag{7}$$

where vector V consists all the measured voltages, $U(\sigma)$ is the FEM solution to the forward problem, and e is additive Gaussian noise with mean e^* and covariance matrix Γ_e. For the details of FEM approximation of CEM, see [56], for example.

III. MOVING MORPHABLE COMPONENTS-BASED SHAPE RECONSTRUCTION FRAMEWORK

In this section, inspired by the work of Guo *et al.* [45], [46], we detail a methodology for describing the geometry of a shape component using explicit parameters. For the sake of simplicity, we only considered two-dimensional (2D) cases in the present work. Extensions to three-dimensional (3D) cases will be studied in a future work. Meanwhile, as a primary attempt to develop the MMC-based reconstruction framework in EIT, a relatively simple form of shape component is introduced here.

Shape and topology are the main concern of the shape-based reconstruction problem. Inasmuch, candidate shape components with simple geometries are selected to serve as basic blocks in the shape and topology optimization based reconstruction method; this selection is of computational importance, especially when the number of candidate components is relatively large. As shown in Fig. 1, even a small number of components can represent fairly complicated shapes and topologies.

A. Shape and Topology Description

In the MMC-based technique, shown in [45], shape and topology can be described implicitly in the following way:

$$\begin{cases} f^s(\boldsymbol{x}) > 0, & \forall \boldsymbol{x} \in D^s, \\ f^s(\boldsymbol{x}) = 0, & \forall \boldsymbol{x} \in \partial D^s, \\ f^s(\boldsymbol{x}) < 0, & \forall \boldsymbol{x} \in \Omega \backslash D^s. \end{cases} \tag{8}$$

Here, $D^s \in \Omega$ denotes a subset of Ω occupied by n components, which is made of the support of the inclusions in the domain Ω. We also have $f^s(\boldsymbol{x}) = \max(f_1, f_2, \cdots, f_n)$ with $f_i = f_i(\boldsymbol{x}), i = 1, 2, \cdots, n$, denoting the shape and topology description function (STDF) of the region occupied by the i^{th} shape component, i.e., D_i, that is,

$$\begin{cases} f_i(\boldsymbol{x}) > 0, & \forall \boldsymbol{x} \in D_i, \\ f_i(\boldsymbol{x}) = 0, & \forall \boldsymbol{x} \in \partial D_i, \\ f_i(\boldsymbol{x}) < 0, & \forall \boldsymbol{x} \in \Omega \backslash D_i. \end{cases} \tag{9}$$

Obviously, $D^s = \cup_{i=1}^{n} D_i$. Fig. 2 provides a schematic illustration of the above geometry representation.

Similar as in [45]–[47], the key idea of the MMC-based approach is to explicitly represent the locations and geometries of shape components with use of a few number of shape 'design variables' (which are used as parameters). As pointed out in [47], we apply the following STDF to represent the locations and geometries of shape components:

$$f_i(x, y) = 1 - \left(\frac{x'}{L_i}\right)^m - \left(\frac{y'}{g(x')}\right)^m, \tag{10}$$

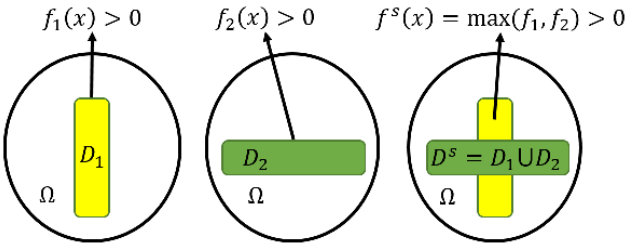

Fig. 2. A schematic illustration of the geometry representation in MMC-based shape reconstruction framework.

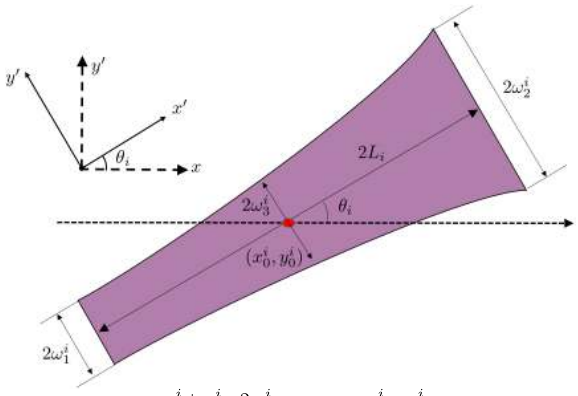

Fig. 3. Geometrical description of a component using quadratically varying thicknesses.

with

$$\begin{bmatrix} x' \\ y' \end{bmatrix} = \begin{bmatrix} \cos(\theta_i) & \sin(\theta_i) \\ -\sin(\theta_i) & \cos(\theta_i) \end{bmatrix} \begin{bmatrix} x - x_0^i \\ y - y_0^i \end{bmatrix}. \tag{11}$$

Here, m is an even number called the exponent, L_i denotes the half length of the component, θ_i is the inclined angle of the component measured from the horizontal axis anti clockwisely, and (x_0^i, y_0^i) denotes the coordinate of the center of the component, respectively. To describe the thickness profile of the component, a function $g(x')$ is introduced and can be taken different forms. For example, Fig. 3 depicts a shape component with quadratically varying thickness. For other forms of $g(x')$, we refer the readers to [46], [50]. Given the quadratically-varying thickness profile of shape components (as shown in Fig.3), we have the shape design variable vector $\boldsymbol{\gamma_i} = (x_0^i, y_0^i, L_i, \theta_i, w_1^i, w_2^i, w_3^i)$ associated with the i^{th} component.

To sum up, with the above geometry representation scheme, the shape and topology of conductivity distribution can be solely determined by the design vector $\boldsymbol{\gamma} = (\boldsymbol{\gamma_1}, \boldsymbol{\gamma_2}, \cdots, \boldsymbol{\gamma_n})^{\mathrm{T}}$.

B. Conductivity Distribution Modeling

Following the common assumption in shape-based reconstruction methods, the conductivity distribution to be reconstructed is assumed to be piece-wise constant. For the sake of brevity, we assume the domain Ω contains two different regions D^s and $\Omega \backslash D^s$ with conductivity profiles as $\sigma(\boldsymbol{x}) = \sigma_1$ for $\boldsymbol{x} \in D^s$ and $\sigma(\boldsymbol{x}) = \sigma_0$ for $\boldsymbol{x} \in \Omega \backslash D^s$.

In association with the two regions represented by the STDF $f^s(\boldsymbol{x})$ using the design vector $\boldsymbol{\gamma} = (\boldsymbol{\gamma_1}, \boldsymbol{\gamma_2}, \cdots, \boldsymbol{\gamma_n})^{\mathrm{T}}$, the interior conductivity distribution $\sigma(\boldsymbol{x})$ in Ω can be described as follows

$$\sigma(\boldsymbol{x}, \boldsymbol{\gamma}) = \sigma_0(1 - H(f^s(\boldsymbol{x}, \boldsymbol{\gamma}))) + \sigma_1 H(f^s(\boldsymbol{x}, \boldsymbol{\gamma})). \tag{12}$$

$H(\xi)$ is the Heaviside function, where $H(\xi) = 0$ for $\xi < 0$ and $H(\xi) = 1$, otherwise.

In practice, one cannot differentiate the exact Heaviside function in the classical sense, thus one often replace it with a smooth approximation of the Heaviside function, such as the C^2 function

$$H_\tau(\xi) = \begin{cases} 0, & \xi < -\tau, \\ \frac{1}{2}[1 + \frac{\xi}{\tau} + \frac{1}{\pi}\sin(\frac{\pi\xi}{\tau})], & |\xi| \le \tau, \\ 1, & \xi > \tau. \end{cases} \tag{13}$$

Here, the positive parameter τ defines a band $\xi_b = 2\tau$ within which the Heaviside function is smoothed.

It is worth remarking that, model (12) in fact maps the space of unknown region D^s into the space of unknown design vector $\boldsymbol{\gamma}$, and is therefore a mechanism for incorporating additional geometric information into shape reconstruction. This feature thereby renders the solution process more flexible, and also reduces the dimension and the complexity of the reconstruction problem.

Finally, the observation model in (7) can be updated as

$$V = U(\sigma(\boldsymbol{x}, \boldsymbol{\gamma})) + e. \tag{14}$$

Then, the shape reconstruction and estimation of piecewise constant conductivity σ_0 and σ_1 in MMC-based approach amounts to solving the minimization problem

$$[\hat{\boldsymbol{\gamma}}, \hat{\sigma}_0, \hat{\sigma}_1] = \arg\min\{\|L_e(V - U(\sigma))\|^2 + \|(\boldsymbol{\gamma} - \boldsymbol{\gamma^*})\|^2 + \sum_{j=0}^{1} \|(\sigma_j - \sigma^*)\|^2\}. \tag{15}$$

Here L_e is defined as $L_e^T L_e = C_e^{-1}$, where C_e is the observation noise covariance matrix. $\boldsymbol{\gamma^*}$ and σ_j^* are predetermined values (see details in Section IV-E). The last two terms on the right-hand side of (15) are referred to as the regularization functionals, promoting stable reconstructions while penalizing unwanted features in the solution.

C. Sensitivity Analysis for MMC-Based Framework

To solve the nonlinear minimization problem in (15), iterative methods (e.g., Gauss-Newton algorithm) are applied. During the iterations, the Jacobian matrix $J(\boldsymbol{\gamma}, \sigma_0, \sigma_1) = \frac{\partial U}{\partial(\boldsymbol{\gamma}, \sigma_0, \sigma_1)}$ is required. We derive the Jacobian by first applying the chain rule which yields

$$J_U(\boldsymbol{\gamma}) = \frac{\partial U}{\partial \boldsymbol{\gamma}} = \frac{\partial U}{\partial \sigma} \cdot \frac{\partial \sigma}{\partial f^s} \cdot \frac{\partial f^s}{\partial \boldsymbol{\gamma}} = \frac{\partial U}{\partial \sigma} \cdot (\sigma_1 - \sigma_0)\delta(f^s) \cdot \frac{\partial f^s}{\partial \boldsymbol{\gamma}}. \tag{16}$$

Here, $\delta(\cdot)$ denotes the Dirac delta function defined as

$$\delta_\tau(\xi) = \frac{d}{d\xi} H_\tau(\xi) = \begin{cases} 0, & |\xi| > \tau, \\ \frac{1}{2\tau}[1 + \cos(\frac{\pi\xi}{\tau})], & |\xi| \le \tau. \end{cases} \tag{17}$$

Jacobian term $\frac{\partial U}{\partial \sigma}$ can be computed using the standard method [14] and $\frac{\partial f^s}{\partial \boldsymbol{\gamma}}$ can be computed analytically.[1]

Similarly, we have

$$J_U(\sigma_0) = \frac{\partial U}{\partial \sigma_0} = \frac{\partial U}{\partial \sigma} \cdot \frac{\partial \sigma}{\partial \sigma_0} = \frac{\partial U}{\partial \sigma} \cdot (1 - H(f^s)), \quad (18)$$

and

$$J_U(\sigma_1) = \frac{\partial U}{\partial \sigma_1} = \frac{\partial U}{\partial \sigma} \cdot \frac{\partial \sigma}{\partial \sigma_1} = \frac{\partial U}{\partial \sigma} \cdot H(f^s). \quad (19)$$

Finally, the minimization problems in (15) is solved with an iterative Gauss-Newton optimization regime, which is equipped with a line-search algorithm to determine the step size λ_k in the solution $\hat{\Theta}_k = \hat{\Theta}_{k-1} + \lambda_k \bar{\Theta}$. Here, $\hat{\Theta}_k$ is the current estimate and $\bar{\Theta}$ is the least squares update.

IV. Methods

In this section, the performance of the MMC-based reconstruction approach is tested with numerical simulations and experimental data. The test cases, implementation details, parameter selection used in the reconstruction and experimental evaluation are explained. For the results and discussion, see Section V

A. EIT Measurement Simulations

To study the performance of the MMC-based approach, three simulated cases, denoted Cases 1-3, were conducted with a thorax-shaped domain obtained from a computed tomography scan of a human thorax. On the domain boundary $L = 16$ electrodes with length 2 cm were equidistantly placed and applied for use in EIT measurements. A total of 54 pairwise current injections were applied between electrodes i and j, $i = 1, 5, 9, 13, j = 1, \ldots, 16 \backslash i$. The amplitude of the current was 1 mA, and the contact impedances z_ℓ were set to 5 $\Omega \cdot$ cm for all the electrodes. The simulated conductivities of the tissues were set as 0.5 mS/cm for lung, 3 mS/cm for heart, 3.1 mS/cm for aorta and 2 mS/cm for background, respectively. The discretization details of the measurement domain are given in Table II. To simulate real conditions, Gaussian noise with 0.1% standard deviation of the difference between the maximum and minimum value of the noiseless data was added to the simulated data. The selected noise level corresponds to the signal to noise ratio SNR = 42 dB.

It is important to remark that in the simulations, we did not use design variables to represent the boundary of regions for assigning conductivity profiles. Rather, the regions of lungs, heart and aorta were identified with the structural mesh.

B. Experimental Setup

In the experimental studies (Cases 4-6), the experiments were conducted with a human thorax-shaped water tank. The horizontal and vertical radii of the tank were $R_h = 17.5$ cm and $R_v = 14$ cm, respectively. Sixteen identical metallic rectangular electrodes with a width of 2 cm were attached to the interior lateral surface of the tank. The tank was filled with saline having a conductivity of 2.05 mS/cm. To simulate different conductivity distributions, lung and heart shaped inclusions made of agar and aorta made of copper were placed inside the tank. Note that more salt was added into the agar gel for making the heart, thereby the conductivity of heart is much higher than lung. The experiments were carried out with KIT4 measurement system [57]. The current patterns described in Section IV-A and adjacent measurement patterns were used in the measurements.

[1]The partial derivatives of f^s with respect to design variables can be found in symbolic form using the *diff* command in `Matlab`

TABLE II
Discretization Details of the Measurement and Reconstruction Domains in the Test Cases. N_u Is the Number of Node Points in the 2nd Order Mesh for Approximation of $u(x)$, and N_σ Is the Number of Node Points for Approximation of $\sigma(x)$ in the 1st Order Mesh

	Simulated data		Reconstruction	
	N_u	N_σ	N_u	N_σ
Cases 1-3	28101	7150	21845	5586
	Experimental data		Reconstruction	
			N_u	N_σ
Cases 4-6			13185	3364

C. Test Cases

To study the performance of the MMC-based method in medical EIT application: lung imaging, the following two types of test cases were carried out.

1) Cases 1&4: Lung Imaging With Homogeneous Background: In this type of test cases, the heart and aorta were assumed to be in an ideal state, having the same conductivity value as the background, i.e., σ_0 is constant.

2) Cases 2-3&5-6: Lung Imaging With Non-Homogeneous Background: From a practical point of view, the heart and aorta have different conductivity profiles compared to the background. For this reason, a more realistic type of test was considered: in Cases 2&5, the heart was assigned or constructed with different conductivity value/material; in Cases 3&6, the heart and aorta were assigned or constructed with different conductivity values/materials. This type of test cases leads to a non-homogeneous background. That is, σ_0 is not constant anymore, leading to modeling errors in MMC-based reconstruction, since the current work is devoted to the problems with single-phase inclusions. We note that it is possible to apply multiple STDFs [53] for representing the regions of lung, heart and aorta. However, as our primary interest in this study is to evaluate the performance of the MMC-based method for lung imaging, we defer this work to the future. The main reason for considering both types is to study the performance of MMC-based method with and without modeling errors due to the non-homogeneous background.

D. Estimates for Comparison

For comparison purposes, we also computed conventional reconstructions based on smoothness prior and total variation prior listed below. For parameter choices in each reconstruction, see Section IV-E.

TABLE III
INITIAL DESIGN VARIABLES USED IN THE MMC-BASED RECONSTRUCTIONS

		Number of components	Center coordinates	Half length L_i	Component thickness ω	θ
Simulations	Right lung	3	$r = 8, \psi = [0, 0.1, 0.2]\pi$	4	$\omega_1^i = \omega_2^i = \omega_3^i \equiv 6, i = 1, 2, 3$	0
	Left lung	3	$r = 8, \psi = [1, 1.1, 1.2]\pi$	4	$\omega_1^i = \omega_2^i = \omega_3^i \equiv 6, i = 4, 5, 6$	0
Experiments	Right lung	3	$r = 8, \psi = [0, 0.1, 0.2]\pi$	7	$\omega_1^i = \omega_2^i = \omega_3^i \equiv 7, i = 1, 2, 3$	0
	Left lung	3	$r = 8, \psi = [0.8, 0.9, 1]\pi$	7	$\omega_1^i = \omega_2^i = \omega_3^i \equiv 7, i = 4, 5, 6$	0

- **Reconstructions based on smoothness prior (SMP)**:

$$\hat{\sigma} = \arg\min_{\sigma>0}\{\|L_e(V - U(\sigma))\|^2 + \|\mathcal{L}_\sigma(\sigma - \sigma^*)\|^2\}, \tag{20}$$

where σ^* is the expectation of σ and $\mathcal{L}_\sigma^{\mathrm{T}}\mathcal{L}_\sigma = \Gamma_\sigma^{-1}$, and Γ_σ is determined element wise, where the matrix element (τ, κ) for a distributed parameter σ at locations x_τ and x_κ is given by

$$\Gamma_\sigma(\tau, \kappa) = a \exp\left\{-\frac{\|x_\tau - x_\kappa\|_2^2}{2b^2}\right\} + d\delta_{\tau\kappa}. \tag{21}$$

Here, the scalars a, b and d are positive, and $\delta_{\tau\kappa}$ denotes the Kronecker delta function, where $\delta_{\tau\kappa} = 1$ for $\tau = \kappa$ and $\delta_{\tau\kappa} = 0$, otherwise. In a basic sense, parameter a contrtols the weighting, b incorporates spatial correlation, and d is a small positive value which is used to ensure that Γ_σ is well-conditioned.

- **Reconstructions based on total variation prior (TVP)**:

$$\hat{\sigma} = \arg\min_{\sigma>0}\{\|L_e(V - U(\sigma))\|^2 + \alpha \mathrm{TV}(\sigma)\}. \tag{22}$$

Here, $\alpha > 0$ is a weighting parameter, and

$$\mathrm{TV}(s) = \sum_{k=1}^{N_e} |e_k| \sqrt{\|(\nabla s)|_{e_k}\|^2 + \beta}$$

is a differentiable approximation of the isotropic total variation functional. $(\nabla s)|_{e_k}$ is the gradient of s at element e_k with $k = 1, 2, \ldots, N_e$, and N_e is the number of elements. $\beta > 0$ is a small positive stabilization parameter.

Note that, in both conventional estimates, the conductivity is reconstructed by treating the internal distribution as continuous i.e. without taking into account the assumption of piecewise constant distributed conductivity. Thus the corresponding unknown parameters vector in SMP and TVP was $\hat{\sigma}^T \in \mathbb{R}^{N_\sigma}$.

E. Implementation Details

In this subsection, we discuss important information related to the implementation of the proposed reconstruction method. To start, we remark that the even number (exponent) m of STDF in (10) was set to 2 in this paper, and $n = 6$ candidate components were used for representing the inclusions shape, except in the robustness study of the proposed approach with respect to different number of components n and exponent m (see details in Sections IV-F & V-B).

The initial candidate components were empirically selected, and the center (x_0, y_0) of initial components were defined by using the polar coordinates r and ψ, i.e., $(x_0, y_0) = (r\cos(\psi), r\sin(\psi))$. Details of the polar coordinates (r, ψ) and other initial design variables of $\boldsymbol{\gamma}^*$ used in the MMC-based reconstructions are listed in Table III. In addition, for shape representation, Heaviside function (13) with $\tau = \mathcal{A}/2$ was used. Here, $\mathcal{A}$ denote the mean value of the element area in the FEM mesh, namely, $\mathcal{A} = \frac{\text{Area of domain } \Omega}{\text{Number of elements}}$.

Next, the expected values σ_0^* and σ_1^* in the penalty term were set to the best homogeneous estimate:

$$\sigma_{\mathrm{hom}} = \arg\min\{\|L_e(V - U(\sigma))\|^2\}. \tag{23}$$

In SMP based reconstruction, to construct the prior covariance in (21), parameters a, b and d were empirically selected as $a = 1.5$ and $a = 9$ for the numerical test cases and experimental test cases, respectively; $b = 3$ and $d = 1 \times 10^{-3}$ are fixed for both numerical and experimental test cases. In TVP based reconstruction, we selected the parameters α and β in (22) by applying a confidence-based strategy studied in [58]. The parameters used in this paper are $\alpha = 0.5$ and $\beta = 1 \times 10^{-3}$, respectively.

F. Robustness Studies

In MMC-based shape reconstruction framework, shape components are served as the basic blocks of shape and topology optimization. Then two natural questions arise here: How many candidate components should be considered in the reconstruction problem, and what is the performance of MMC-based reconstruction when the exponent m of STDF increases? For example, in some cases one might also be interested to check the performance with components number n more than six and exponent m bigger than two. To get insight to these questions, we carried out a set of reconstructions of Case 1 using $n = 6, 8, 12$ and 24 with a fixed exponent $m = 2$ to investigate how the number of components n influences the reconstruction; we also carried out a set of reconstructions of Case 1 using different exponent $m = 2, 4, 6$ and 8 with a fixed number of components $n = 6$.

Note that studying the performance of the proposed approach by varying the component's number n could be treated as an alternative way to check the performance of the approach *w.r.t* different expected values of $\boldsymbol{\gamma}^*$ in the minimization problem of (15). Further, to explore the effect of initial piecewise constant conductivity values in (15) for the proposed approach, we performed a set of reconstructions of Case 1 by assigning different values to σ^*. For this purpose, we define

$$\sigma^* = \eta\sigma_{\mathrm{hom}}, \tag{24}$$

TABLE IV
EVALUATION CRITERIA IN SIMULATED TEST CASES: SSIMS AND RCOS

	Case 1			Case 2			Case 3		
	SSIM	RCoσ_0	RCoσ_1	SSIM†	RCoσ_0	RCoσ_1	SSIM†	RCoσ_0	RCoσ_1
True	1.00	1.00	1.00	1.00	1.00	1.00	1.00	1.00	1.00
MMC	0.96	1.00	1.01	0.92	1.01	0.95	0.92	1.01	0.96
SMP	0.76	-	-	0.77	-	-	0.78	-	-
TVP	0.80	-	-	0.85	-	-	0.84	-	-

† The true image of Case 1 was used as the reference image for calculating SSIMs of MMC-based reconstructions in Cases 2&3 to avoid the influence arising from the heart and aorta regions, since our primary interest in these test cases is to recover the lung shape.

TABLE V
EVALUATION CRITERIA FOR EXPERIMENTAL STUDIES: RCOS AND RCRS

	Case 4			Case 5			Case 6		
	RCR_L^*	RCR_R^*	RCoσ_0	RCR_L	RCR_R	RCoσ_0	RCR_L	RCR_R	RCoσ_0
True	1.00	1.00	1.00	1.00	1.00	1.00	1.00	1.00	1.00
MMC	0.99	0.96	1.00	0.91	0.81	0.99	0.90	0.80	0.97
SMP	1.05	1.12	-	1.02	1.07	-	1.02	1.06	-
TVP	0.73	0.72	-	0.70	0.70	-	0.69	0.68	-

* The subscript letters 'L' and 'R' under the parameter RCR denote the left and right side lungs in the tank, respectively.

where η is the initial conductivity coefficient. With $\eta = [0.2, 0.4, \cdots, 2]$, a total of 10 images were obtained. The evaluation parameters described in Section IV-G versus η were computed for all the images and are shown in Fig.10.

G. Evaluation Criteria

To evaluate the performance of the proposed approach we apply some criteria measuring the reconstruction ability. First, to access quantitatively the recovery of binary conductivity values, we calculated a relative contrast (RCo):

$$\text{RCo}\sigma_j = \frac{\widehat{\sigma_j}}{\sigma_j^{\text{True}}}. \tag{25}$$

To allow easy comparison of the values in Tables IV & V, the relative quantity RCo was used here instead of the respective quantity $\widehat{\sigma_j}$. For RCo, a value of 1 would indicate exact match of the true and estimated binary conductivity values, while a value greater or less than 1 would indicate overestimation or underestimation, respectively. As mentioned in Section IV-D, the internal conductivity distribution was treated as continuous in the SMP and TVP-based estimates. Therefore, we didn't compute RCo for both reference estimates. As an additional metric, we utilize the structural similarity (SSIM) for measuring the similarity between the true and reconstructed images in the numerical test cases for all the estimates.

To quantitatively access the recovery of the shape in the experimental studies, we computed the relative area coverage ratio (RCR), shown in Table V, for the inclusions in the reconstructed images:

$$\text{RCR} = \frac{\text{CR}}{\text{CR}_{\text{True}}}, \tag{26}$$

where CR denotes the coverage ratio defined as the ratio of the area of the recovered inclusions to the total area of the water tank. Correspondingly, CR_{True} is the CR of the true inclusion. Value one would indicate exact match of area of the recovered and true inclusions, while a value less or greater than one would indicate underestimation or overestimation, respectively.

Note that, for the experimental studies, 75% of the measured saline conductivity was applied as the threshold for detecting the inclusions, and ImageJ was used to determine the approximated true areas of the lung-shaped inclusions.

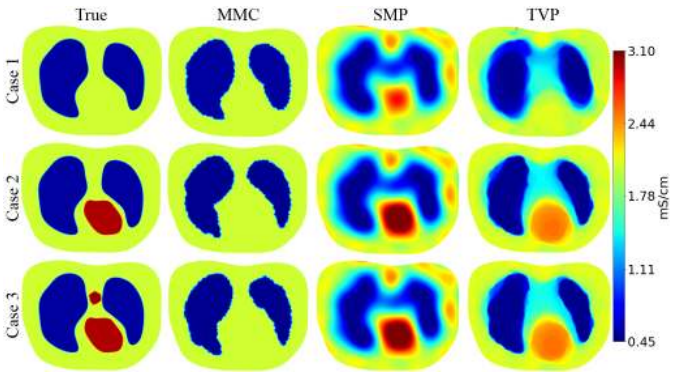

Fig. 4. Reconstructions of Cases 1-3 using simulated data. All the images have color bar scale from 0.45 mS/cm to 3.10 mS/cm.

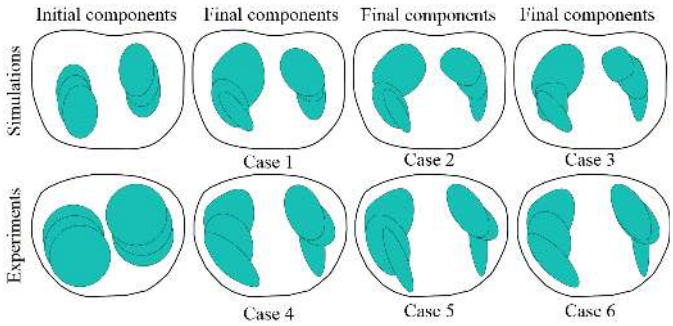

Fig. 5. Plots of initial candidate components and final components in Cases 1-6 with MMC-based approach.

V. RESULTS

In this section, we first show the MMC-based reconstructions for numerical test cases. Then, robustness studies of the proposed approach against different component numbers, exponent in the STDF as well as modeling errors caused by the presence of non-homogeneous background are presented. Finally, experimental data is used for investigating the performance of the proposed approach.

A. Reconstructions From Simulated Data

Fig. 4 shows the results of test Cases 1-3: the images on the first column denote the (simulated) true conductivity distributions; the final MMC-based reconstructions are shown in the second column; The conventional reconstructions SMP and TVP are shown in the third and last columns, respectively. Note that the initial and final component distributions of MMC-based approach in Cases 1-3 are shown in the first row of Fig. 5.

We observe that the conventional approaches (SMP and TVP) and the proposed MMC-based approach successfully detect the inclusions and track the shape of the lung relatively well. However, the quality of the estimates obtained with the proposed MMC approach and TVP are visibly superior to quality of SMP estimate. The SMP estimate, on the other hand, produces artifacts that appear in the domain as blurred anomalies, making it difficult to track a clear interface between lungs and background. This is an expected result, since the true conductivity is piecewise constant distributed, i.e., the

conductivity is discontinuous, so the selected smoothness prior of SMP is obviously not the best option in these test cases. In other words, the assumption of smoothness in not realistic.

On the other hand, MMC-based estimate provides quantitatively accurate reconstructions for the shape of lungs and the binary conductivities, In overall, MMC-based estimate is more reliable than SMP and at least comparable to TVP, which is especially evident with the best SSIM parameter listed in Table IV.

Further, when there is modeling error (caused by non-homogeneous background) presented in the reconstruction problem of Cases 2&3, the MMC-based estimate still gives feasible reconstructions of the lung. This is mainly because the EIT measurement data is more sensitive to large inclusions with low conductivity and is relatively insensitive to small inclusions with high conductivity presented in the domain. For example, in real medical applications, lungs are less conductive than the background due to the presence of air. Moreover, the size of the heart and/or aorta is significantly smaller than the lungs while the conductivity is higher. It is therefore apparent that there is a trade-off between the sizes and relative conductivities present in the background, heart, aorta and lungs. For this reason, the heart and aorta are 'absorbed' by the background during the reconstruction automatically. These findings and features are accordance to our previous works using PLS-based reconstructions [23] and [43]. In some special cases, as mentioned in Section IV-C, one may apply two or three STDFs [53] for representing the regions of lung, heart and aorta, respectively. A general strategy for representing multiple regions using multiple STDFs will be discussed in Section V-D.

Note that, for the sake of comparison to other shape-based estimate, we recall our previous results for the same test Cases 1&2 using PLS method in Fig.7 of [23]. The MMC-based estimate is slightly better than the PLS-based estimate, e.g., in Case 2, SSIM for MMC-based estimate is 0.92 and that one for PLS-based estimate is 0.91. Since both values are very close to the true value one, we believe that both methods have a similar performance and are comparable to each other in terms of image quality.

Fig. 6 shows the evolution of components during the shape optimization process of Case 1. From this figure it can be clearly observed how the final shape and topology of the inclusions are progressively reached by updating the positions and shapes of the components.

To see how are the binary conductivity values σ_j updated in the MMC-based reconstruction, in Fig. 7(left) we show the comparisons between the true and estimated binary conductivity values at each iteration. To check the convergence behaviors of the MMC-based approach, the root mean square error (RMSE) between the estimated conductivity distribution $\hat{\sigma}(\boldsymbol{x}, \boldsymbol{\gamma})$ and the true $\sigma(\boldsymbol{x})$ was computed as

$$\text{RMSE} = \frac{\|P\sigma(\boldsymbol{x}) - \hat{\sigma}(\boldsymbol{x}, \boldsymbol{\gamma})\|^2}{\|P\sigma(\boldsymbol{x})\|^2} \times 100\%, \tag{27}$$

where P is a matrix that interpolates $\sigma(\boldsymbol{x})$ from a fine mesh onto a coarse mesh. The RMSE versus the number of iteration steps is shown in Fig. 7(right).

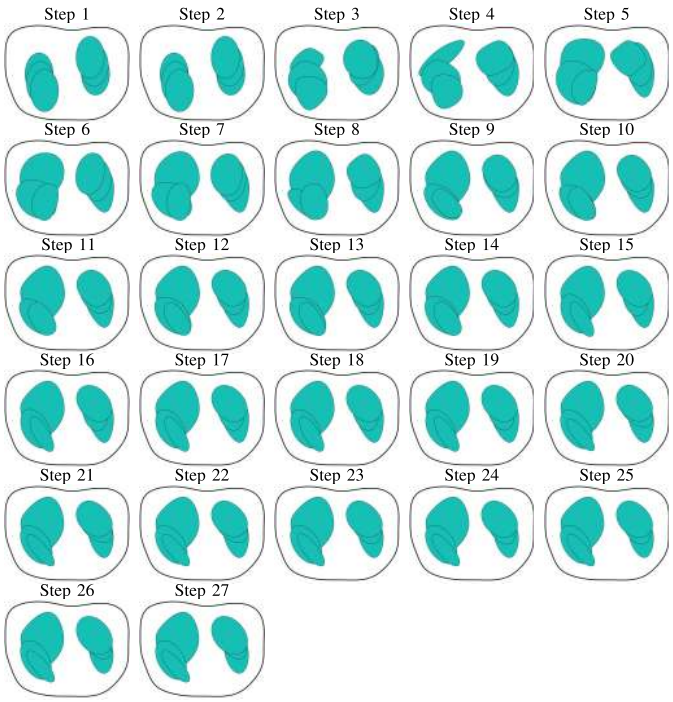

Fig. 6. Evolution of candidate components during the shape optimization process in Case 1.

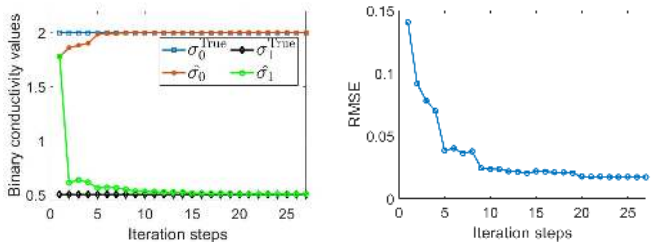

Fig. 7. Estimation of binary conductivity values and RMSE versus number of iteration steps for the MMC-based reconstruction in Case 1.

B. Results of Robustness Studies

Fig. 8 investigates how the number of candidate components n influences the reconstruction. As can be seen from Fig. 8, estimates with $n = 6, 8$ and 12 well recover the lung shape and binary conductivity values, leading to evaluation criteria very close to the true value one, see details in bottom row of Fig. 8. On the other hand, when more candidate components are considered, e.g., n is chosen to be 24, the geometry of the shape becomes severely distorted and the conductivity of the inclusion is significantly overestimated. This feature does not go beyond our expectation, since estimate with a large number of n will inevitably increase the number of (unknown) design variables. For example, the dimension of unknown design variable vector $\boldsymbol{\gamma}$ is 24×7 for $n = 24$. In fact, by increasing the number of candidate components, not only the reconstruction problem becomes increasingly *ill-posed* and more computationally demanding, the size of the solution space also increases [59].

Fig. 9 illustrates the sensitivity of the reconstruction scheme against the choice of the even number (exponent) m in STDF. It can be seen that the estimate with $m = 2$ shows superior performance and tracks the shape of the inclusions remarkably

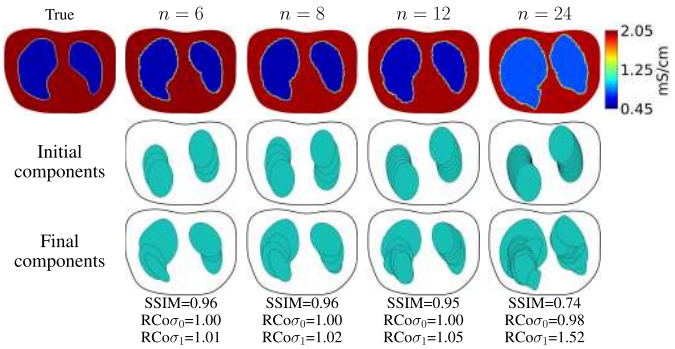

Fig. 8. Robustness study of the MMC-based estimate with respect to the number of components n. The same data of Case 1 and exponent $m = 2$ were used for the reconstruction. The second column with $n = 6$ is a repetition of the first row in Fig. 4 but with different color bar range.

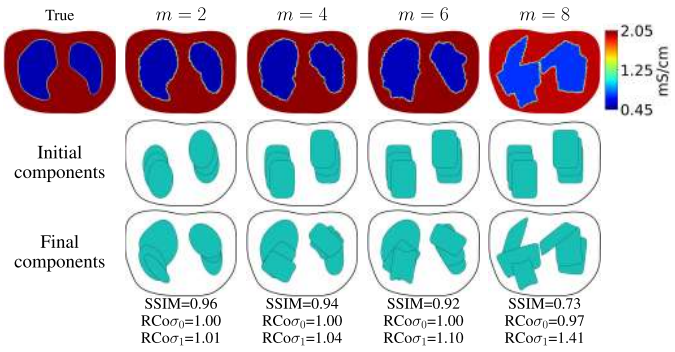

Fig. 9. Robustness study of the MMC-based estimate with respect to exponent m. The same data of Case 1 and component number $n = 6$ were used for the reconstruction. The second column with $m = 2$ is also a repetition of the first row in Fig. 4 but with different color bar range.

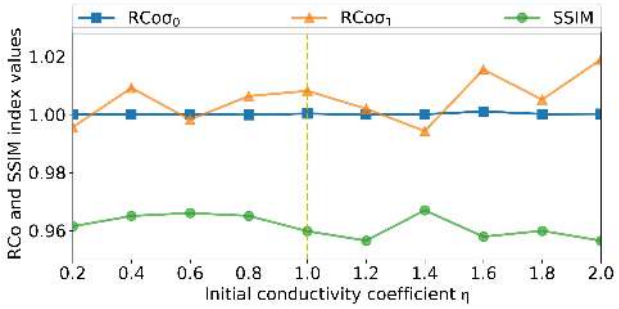

Fig. 10. Evaluation parameters of the robustness study of the MMC-based approach versus the initial conductivity coefficient η. The same data set as Case 1 was used for the reconstruction. The dashed vertical line denotes the case shown in Fig. 4.

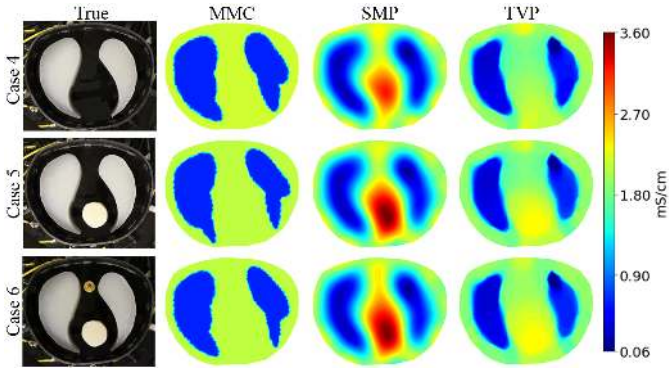

Fig. 11. Reconstructions of Cases 4-6 using experimental data. In Cases 5&6, the conductivity of lung is entirely different from the heart because more salt has been added to the agar gel to make the heart.

well, as evidenced by the evaluation parameters shown in the bottom row of Fig.9. On the other hand, edge serrations are produced when m increases, causing shape distortions to the reconstructed images.

The second row of Fig.9 illustrates how, as the exponent m increases, the initial candidate components gradually change from ellipses to rounded rectangles. In fact, as the exponent m approaches a relatively large value, the candidate components become possessing sharp corners. From experience with medical applications, organ and inclusions in the body are often smooth, therefore, m should be selected in such a way that it will allow the candidate components to possess smooth boundaries (e.g., edges with relatively large radii). However, if one is interested in reconstructing inclusions that may have sharp corners, a relatively large value of m should be utilized. For example, in the well-studied examples of structure topology optimization [45], [46], [53], m was set to six.

Fig. 10 shows the evaluation criteria of the robustness study of the proposed approach against different initial piecewise constant conductivity values σ^*. Based on these results, we can conclude that the proposed approach is quite robust to the varying initial σ^*, resulting very good reconstructions of the lung shape and estimation of the binary conductivity values.

C. Reconstructions From Experimental Data

Next, we proceed to reconstructions from water tank data. Fig. 11 depicts the results of Cases 4-6 described in Section IV-C. The initial candidate and final components are shown in the second row of Fig. 5. The contrast RCo based on MMC estimate for background, i.e., saline, and the coverage ratios based on the estimates (MMC, SMP and TVP), of the lung-shaped inclusions are tabulated in Table V. Note that we only show the RCo for the background with MMC based estimate, since the exact conductivity values of the lung-shaped inclusions were not known. Also, as mentioned in Section IV-D, in the estimates with SMP and TVP, the internal conductivity distribution was treated as continuous, such that RCo is not available for both reference estimates.

As the results shown in Fig. 11, all the estimates are able to recover the shape and location of lung-shaped inclusions relatively well. However, the quality of the estimate obtained with the proposed MMC approach is better compared to the estimates using SMP and TVP. The coverage ratio RCR (26) with MMC is very close to the true value in Case 4, see Table V. Meanwhile, the boundaries of the lung-shaped inclusions are sharper than in the estimates with SMP and TVP. Despite the modeling error (caused by non-homogeneous background) presented in the reconstruction problem of Cases 5&6, the MMC-based estimate still provides feasible reconstructions of the lung-shaped inclusions. This is also consistent with the results of Cases 1-3 in Section V-A. We note that the RCRs of Cases 5&6 in Table V are slightly underestimated, which does not exceed our expectation, due to the modeling errors caused by the non-homogeneous background.

D. Limitations and Further Developments

The present framework is limited by the fact that it is based on the context of *absolute imaging*. As such, a number of issues need to be mentioned.

- First, it is well known that, for absolute imaging, the use of non-linear iterative methods coupled with a line search takes several minutes or hours to obtain the final reconstructions. As an example, the final reconstructions of SMP and TVP shown Case 1 were obtained from a MATLAB implementation of the estimates described in Section IV-D on a desktop PC with an Intel Core i7-6700K processor and 32GB memory within 9 iterations at average speed of 6.7 minutes/iteration, and 8 iterations at average speed of 35 minutes/iteration, respectively.
  We would like to point out that the proposed MMC-based approach holds the potential to improve the conditional number of the reconstruction problem and also to reduce the computational demand associated with shape reconstruction. As a demonstration of this realization, in Case 1, the MMC-based estimate was obtained from a MATLAB implementation of the proposed approach on the above PC within 27 iterations at average speed of 4.5 minutes/iteration. Note that, in fact, in MMC reconstruction, the updates after 9 iterations become sufficiently small to reach the stopping criteria. Even though the MMC-based iteration process is faster than SMP and TVP-based estimates, this still makes the usage of the MMC-based shape reconstruction in real-time prohibitive. It is highly desirable to develop a methodology, in principle, that uses the MMC-based technique, which can be deployed in real-time. As a potential solution to improve the efficiency, the proposed algorithm can be accelerated using more efficient forward solvers and more advanced optimization methods. Possible approaches to accelerate the minimization include approximation error model [60] and also reduced order models [61] to speed up the inversion. This would be crucial with a view to practical medical applications.
- Second, to speedup the reconstruction, another option is to formulate the MMC-based reconstruction approach in the context of *linear difference imaging*, since it is known that the shape information in EIT is some sense invariant under linearization [62]. Generally, in difference imaging, the nonlinear forward problem $U(\sigma)$ is linearized at a (homogeneous) conductivity distribution σ_{hom} by using the first order Taylor series: $U(\sigma) \approx U(\sigma_{\text{hom}}) + J_U(\sigma_{\text{hom}})(\sigma - \sigma_{\text{hom}})$. Then, by fixing the Jacobian term $J_U(\sigma_{\text{hom}})$, the support of the conductivity difference $\Delta\sigma(\boldsymbol{x}, \boldsymbol{\gamma}) = \sigma - \sigma_{\text{hom}}$ can be obtained through solving a least square based minimization problem and updating the Jacobian $J_{\Delta\sigma}(\boldsymbol{\gamma})$, for example. Since $J_U(\sigma_{\text{hom}})$ can be computed off-line, it can significantly speed up the MMC-based reconstruction. We defer the details of studying the new MMC-based difference imaging approach to future work.
- Third, in the robustness studies of the proposed approach with non-homogeneous background by presenting a heart and/or aorta in the measurement domain, the main interest in these studies is to track the lung shape. However, a natural question that arises here is whether the proposed MMC-based approach is capable of reconstructing the heart and/or aorta instead of lung? Here, we address this question by recalling the common phenomenon: EIT measurement is more sensitive to large inclusions with low conductivity and is relatively insensitive to small inclusions with high conductivity. Considering that in the real applications, lungs are resistive due to presence of air, conductivity contrast of lung is quite high with respect to background, and heart/aorta size is significantly small compared to lung, such that the corresponding voltages induced by lung have more effect than that of heart or aorta on the EIT measurements. Therefore, the heart and aorta are 'absorbed' by the background during the reconstruction automatically. However, for some special cases, one may apply multiple STDFs to do multiphase estimation for both shapes of lung and heart/aorta.

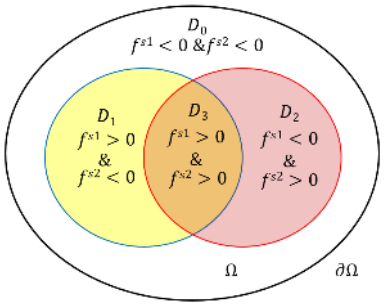

Fig. 12. Modeling multiple regions with STDFs. Each region is characterized by a different sign combination of the two STDFs $f^{s1}(\boldsymbol{x},\boldsymbol{\gamma}^1)$ and $f^{s2}(\boldsymbol{x},\boldsymbol{\gamma}^2)$.

In multiphase estimation, the key point is to model the conductivity distribution by using some characteristic functions, e.g., multiple STDFs. Similar as in [43], a number of p STDFs can be used to represent up to $\omega = 2^p$ different phases by distinguishing all possible sign combinations of these STDFs. For sake of simplicity, we illustrate the idea with the simple but representative case where $p = 2$. Suppose, there are four regions/phases in the domain with piecewise constant conductivity values of regions as $\sigma = (\sigma_0, \sigma_1, \sigma_2, \sigma_3)$. The four regions/phases are represented by two STDFs $f^{s1}(\boldsymbol{x}, \boldsymbol{\gamma^1})$ and $f^{s2}(\boldsymbol{x}, \boldsymbol{\gamma^2})$ that can be described through inner conductivity distribution $\sigma(\boldsymbol{x}, \boldsymbol{\gamma^1}, \boldsymbol{\gamma^2})$ as

$$\begin{aligned}\sigma(\boldsymbol{x}, \boldsymbol{\gamma^1}, \boldsymbol{\gamma^2}) = {} & \sigma_0(1-H(f^{s1}(\boldsymbol{x}, \boldsymbol{\gamma^1})))(1-H(f^{s2}(\boldsymbol{x}, \boldsymbol{\gamma^2}))) \\ & + \sigma_1 H(f^{s1}(\boldsymbol{x}, \boldsymbol{\gamma^1}))(1 - H(f^{s2}(\boldsymbol{x}, \boldsymbol{\gamma^2}))) \\ & + \sigma_2(1 - H(f^{s1}(\boldsymbol{x}, \boldsymbol{\gamma^1})))H(f^{s2}(\boldsymbol{x}, \boldsymbol{\gamma^2})) \\ & + \sigma_3 H(f^{s1}(\boldsymbol{x}, \boldsymbol{\gamma^1}))H(f^{s2}(\boldsymbol{x}, \boldsymbol{\gamma^2})).\end{aligned}$$

Fig.12 outlines a general idea on how two STDFs $f^{s1}(\boldsymbol{x}, \boldsymbol{\gamma^1})$ and $f^{s2}(\boldsymbol{x}, \boldsymbol{\gamma^2})$ are used in this strategy for representing four different regions, in which $\sigma|_{D_j} = \sigma_j, j = 0, \cdots, 3$. We remark that, studying the implementation of MMC-based multiphase reconstruction

framework is out of the scope of this paper, hence it was left as a future research.

- Lastly, the proposed reconstruction approach is based in the framework of *absolute imaging* and is still in its infancy. As such, much additional work needs to be done to improve its efficiency, and to explore its robustness to modeling error, e.g., errors due to inaccurately known contact impedances and domain boundary shape. We are currently extending the proposed framework to *difference imaging* to reduce stringency with respect to the requirement for accurate knowledge of the domain boundary shape ever-present in *absolute imaging*. Clearly, this matter is beyond the scope of this paper and is planned to be presented in a future work. Moreover, for sake of simplicity in this paper we considered only 2D problems, whereas the capability and efficiency of the proposed framework is more pronounced for 3D shape reconstructions where the contrast between the number of voxels and the number of design variable parameters in a MMC-based approach is more significant. Studying 3D scenarios via the propose framework is an important future direction and a continuation of the current work.

VI. Conclusion

In this paper, we proposed a moving morphable component-based framework for the EIT shape-reconstruction problem. In this effort, we demonstrated shape reconstruction in an explicit and geometrical way using the proposed approach. The key idea of the proposed approach is that a set of morphable components represented by STDFs with variable parameters (such as lengths, thicknesses, orientations) is treated as the basic blocks of shape reconstruction. The optimal conductivity distribution, i.e., geometric shape, is found by optimizing STDF parameters and layout (connectivity) of these morphable components. Moreover, based on the fact that the number of underlying parameters in the proposed approach are usually much less than those involved in traditional STDF-based approaches, the conditional number of the reconstruction problem is intrinsically improved. In particular, the proposed framework offers a mechanism to directly and effectively incorporate prior information, such as position, size, etc., of the inclusions to be imaged into the reconstruction problem, which may has practical advantages in medical applications.

Acknowledgment

The authors would like to thank Danny Smyl, PhD for the helpful discussions.

References

[1] K. Y. Aristovich, B. C. Packham, H. Koo, G. S. D. Santos, A. McEvoy, and D. S. Holder, "Imaging fast electrical activity in the brain with electrical impedance tomography," *NeuroImage*, vol. 124, pp. 204–213, Jan. 2016.

[2] A. Adler and A. Boyle, "Electrical impedance tomography: Tissue properties to image measures," *IEEE Trans. Biomed. Eng.*, vol. 64, no. 11, pp. 2494–2504, Nov. 2017.

[3] E. K. Murphy, A. Mahara, and R. J. Halter, "Absolute reconstructions using rotational electrical impedance tomography for breast cancer imaging," *IEEE Trans. Med. Imag.*, vol. 36, no. 4, pp. 892–903, Apr. 2017.

[4] J. L. Mueller *et al.*, "Estimating regions of air trapping from electrical impedance tomography data," *Physiol. Meas.*, vol. 39, no. 5, 2018, Art. no. 05NT01.

[5] M. Wang, Q. Wang, and B. Karki, "Arts of electrical impedance tomographic sensing," *Philos. Trans. Roy. Soc. A*, vol. 374, no. 2070, 2016, Art. no. 20150329.

[6] J. Yao and M. Takei, "Application of process tomography to multiphase flow measurement in industrial and biomedical fields: A review," *IEEE Sensors J.*, vol. 17, no. 24, pp. 8196–8205, Dec. 2017.

[7] D. Smyl, M. Pour-Ghaz, and A. Seppänen, "Detection and reconstruction of complex structural cracking patterns with electrical imaging," *NDT E Int.*, vol. 99, pp. 123–133, Oct. 2018.

[8] D. Liu, V. Kolehmainen, S. Siltanen, A.-M. Laukkanen, and A. Seppänen, "Nonlinear difference imaging approach to three-dimensional electrical impedance tomography in the presence of geometric modeling errors," *IEEE Trans. Biomed. Eng.*, vol. 63, no. 9, pp. 1956–1965, Sep. 2016.

[9] S. Liu, J. Jia, Y. D. Zhang, and Y. Yang, "Image reconstruction in electrical impedance tomography based on structure-aware sparse Bayesian learning," *IEEE Trans. Med. Imag.*, vol. 37, no. 9, pp. 2090–2102, Sep. 2018.

[10] M. Alsaker and J. L. Mueller, "Use of an optimized spatial prior in d-bar reconstructions of EIT tank data," *Inverse Problems Imag.*, vol. 12, no. 4, pp. 883–901, 2018.

[11] S. J. Hamilton, J. L. Mueller, and M. Alsaker, "Incorporating a spatial prior into nonlinear D-bar EIT imaging for complex admittivities," *IEEE Trans. Med. Imag.*, vol. 36, no. 2, pp. 457–466, Feb. 2017.

[12] V. Kolehmainen, M. J. Ehrhardt, and S. R. Arridge, "Incorporating structural prior information and sparsity into EIT using parallel level sets," *Inverse Problems Imag.*, vol. 13, no. 2, pp. 285–307, 2019.

[13] Z. Wei, D. Liu, and X. Chen, "Dominant-current deep learning scheme for electrical impedance tomography," *IEEE Trans. Biomed. Eng.*, to be published. doi: 10.1109/TBME.2019.2891676

[14] M. Vauhkonen, D. Vadasz, P. A. Karjalainen, E. Somersalo, and J. P. Kaipio, "Tikhonov regularization and prior information in electrical impedance tomography," *IEEE Trans. Med. Imag.*, vol. 17, no. 2, pp. 285–293, Apr. 1998.

[15] J. L. Mueller and S. Siltanen, *Linear and Nonlinear Inverse Problems With Practical Applications*, vol. 10. Philadelphia, PA, USA: SIAM, 2012.

[16] D. Liu, V. Kolehmainen, S. Siltanen, and A. Seppänen, "A nonlinear approach to difference imaging in EIT; assessment of the robustness in the presence of modelling errors," *Inverse Problems*, vol. 31, no. 3, 2015, Art. no. 035012.

[17] D. Liu, V. Kolehmainen, S. Siltanen, A.-M. Laukkanen, and A. Seppänen, "Estimation of conductivity changes in a region of interest with electrical impedance tomography," *Inverse Problems Imag.*, vol. 9, no. 1, pp. 211–229, 2015.

[18] K. Lee, E. J. Woo, and J. K. Seo, "A fidelity-embedded regularization method for robust electrical impedance tomography," *IEEE Trans. Med. Imag.*, vol. 37, no. 9, pp. 1970–1977, Sep. 2018.

[19] X. Chen, *Computational Methods for Electromagnetic Inverse Scattering*. Hoboken, NJ, USA: Wiley, 2018.

[20] B. Harrach, "Recent progress on the factorization method for electrical impedance tomography," *Comput. Math. Methods Med.*, vol. 2013, Mar. 2013, Art. no. 425184.

[21] A. K. Khambampati, Y. J. Hong, K. Y. Kim, and S. Kim, "A boundary element method to estimate the interfacial boundary of two immiscible stratified liquids using electrical resistance tomography," *Chem. Eng. Sci.*, vol. 95, pp. 161–173, May 2013.

[22] A. K. Khambampati, K. Y. Kim, Y.-G. Lee, and S. Kim, "Boundary element method to estimate the time-varying interfacial boundary in horizontal immiscible liquids flow using electrical resistance tomography," *Appl. Math. Model.*, vol. 40, no. 2, pp. 1052–1068, 2016.

[23] D. Liu, A. K. Khambampati, and J. Du, "A parametric level set method for electrical impedance tomography," *IEEE Trans. Med. Imag.*, vol. 37, no. 2, pp. 451–460, Feb. 2018.

[24] S. Ren, M. Soleimani, Y. Xu, and F. Dong, "Inclusion boundary reconstruction and sensitivity analysis in electrical impedance tomography," *Inverse Problems Sci. Eng.*, vol. 26, no. 7, pp. 1037–1061, 2018.

[25] E. Beretta, S. Micheletti, S. Perotto, and M. Santacesaria, "Reconstruction of a piecewise constant conductivity on a polygonal partition via shape optimization in EIT," *J. Comput. Phys.*, vol. 353, pp. 264–280, Jan. 2018.

[26] D. Liu, D. Smyl, and J. Du, "A parametric level set-based approach to difference imaging in electrical impedance tomography," *IEEE Trans. Med. Imag.*, vol. 38, no. 1, pp. 145–155, Jan. 2019.

[27] S. Ren, K. Sun, D. Liu, and F. Dong, "A statistical shape constrained reconstruction framework for electrical impedance tomography," *IEEE Trans. Med. Imag.*, to be published. doi: 10.1109/TMI.2019.2900031

[28] D. Liu, D. Gu, D. Smyl, J. Deng, and J. Du, "B-spline based sharp feature preserving shape reconstruction approach for electrical impedance tomography," *IEEE Trans. Med. Imag.*, to be published. doi: 10.1109/TMI.2019.2905245.

[29] A. Kirsch, "Characterization of the shape of a scattering obstacle using the spectral data of the far field operator," *Inverse Problems*, vol. 14, no. 6, p. 1489, 1998.

[30] B. Gebauer and N. Hyvönen, "Factorization method and irregular inclusions in electrical impedance tomography," *Inverse Problems*, vol. 23, no. 5, p. 2159, 2007.

[31] B. Harrach and M. N. Minh, "Enhancing residual-based techniques with shape reconstruction features in electrical impedance tomography," *Inverse Problems*, vol. 32, no. 12, 2016, Art. no. 125002.

[32] B. Harrach and M. N. Minh, "Monotonicity-based regularization for phantom experiment data in electrical impedance tomography," in *New Trends in Parameter Identification for Mathematical Models*. Cham, Switzerland: Springer, 2018, pp. 107–120.

[33] L. Zhou, B. Harrach, and J. K. Seo, "Monotonicity-based electrical impedance tomography for lung imaging," *Inverse Problems*, vol. 34, no. 4, Mar. 2018, Art. no. 045005.

[34] M. Ikehata, "Enclosing a polygonal cavity in a two-dimensional bounded domain from cauchy data," *Inverse Problems*, vol. 15, no. 5, p. 1231, 1999.

[35] M. Ikehata and S. Siltanen, "Numerical method for finding the convex hull of an inclusion in conductivity from boundary measurements," *Inverse Problems*, vol. 16, no. 4, p. 1043, 2000.

[36] M. Alsaker, S. J. Hamilton, and A. Hauptmann, "A direct D-bar method for partial boundary data electrical impedance tomography with *a priori* information," *Inverse Problems Imag.*, vol. 11, no. 3, pp. 427–454, 2017.

[37] M. Soleimani, W. R. B. Lionheart, and O. Dorn, "Level set reconstruction of conductivity and permittivity from boundary electrical measurements using experimental data," *Inverse Problems Sci. Eng.*, vol. 14, no. 2, pp. 193–210, 2006.

[38] D. Liu, A. K. Khambampati, S. Kim, and K. Y. Kim, "Multi-phase flow monitoring with electrical impedance tomography using level set based method," *Nucl. Eng. Des.*, vol. 289, pp. 108–116, Aug. 2015.

[39] F. Gibou, R. Fedkiw, and S. Osher, "A review of level-set methods and some recent applications," *J. Comput. Phys.*, vol. 353, pp. 82–109, Jan. 2018.

[40] M. Y. Wang and S. Wang, "Parametric shape and topology optimization with radial basis functions," in *Proc. IUTAM Symp. Topol. Design Optim. Struct., Mach. Mater.* Dordrecht, The Netherlands: Springer, 2006, pp. 13–22.

[41] L. Jiang, S. Chen, and P. Wei, "Concurrent optimization of structure topology and infill properties with a cardinal-function-based parametric level set method," in *Proc. ASME Int. Design Eng. Tech. Conf. Comput. Inf. Eng. Conf.*, American Society of Mechanical Engineers, 2018, Art. no. V02BT03A006.

[42] A. Kadu, T. van Leeuwen, and W. A. Mulder, "Salt reconstruction in full-waveform inversion with a parametric level-set method," *IEEE Trans. Comput. Imag.*, vol. 3, no. 2, pp. 305–315, Jun. 2017.

[43] D. Liu, Y. Zhao, A. K. Khambampati, A. Seppänen, and J. Du, "A parametric level set method for imaging multiphase conductivity using electrical impedance tomography," *IEEE Trans. Comput. Imag.*, vol. 4, no. 4, pp. 552–561, Dec. 2018.

[44] A. Aghasi, M. Kilmer, and E. L. Miller, "Parametric level set methods for inverse problems," *SIAM J. Imag. Sci.*, vol. 4, no. 2, pp. 618–650, 2011.

[45] X. Guo, W. Zhang, and W. Zhong, "Doing topology optimization explicitly and geometrically—A new moving morphable components based framework," *J. Appl. Mech.*, vol. 81, no. 8, 2014, Art. no. 081009.

[46] X. Guo, W. Zhang, J. Zhang, and J. Yuan, "Explicit structural topology optimization based on moving morphable components (MMC) with curved Skeletons," *Comput. Methods Appl. Mech. Eng.*, vol. 310, pp. 711–748, Oct. 2016.

[47] W. Zhang, J. Yuan, J. Zhang, and X. Guo, "A new topology optimization approach based on moving morphable components (MMC) and the ersatz material model," *Struct. Multidisciplinary Optim.*, vol. 53, no. 6, pp. 1243–1260, 2016.

[48] W. Zhang, J. Zhang, and X. Guo, "Lagrangian description based topology optimization—A revival of shape optimization," *J. Appl. Mech.*, vol. 83, no. 4, 2016, Art. no. 041010.

[49] X. Guo, J. Zhou, W. Zhang, Z. Du, C. Liu, and Y. Liu, "Self-supporting structure design in additive manufacturing through explicit topology optimization," *Comput. Methods Appl. Mech. Eng.*, vol. 323, pp. 27–63, Aug. 2017.

[50] W. Zhang *et al.*, "Explicit three dimensional topology optimization via moving morphable void (MMV) approach," *Comput. Methods Appl. Mech. Eng.*, vol. 322, pp. 590–614, Aug. 2017.

[51] W. Zhang, W. Yang, J. Zhou, D. Li, and X. Guo, "Structural topology optimization through explicit boundary evolution," *J. Appl. Mech.*, vol. 84, no. 1, 2017, Art. no. 011011.

[52] W. Zhang, D. Li, J. Yuan, J. Song, and X. Guo, "A new three-dimensional topology optimization method based on moving morphable components (MMCs)," *Comput. Mech.*, vol. 59, no. 4, pp. 647–665, 2017.

[53] W. Zhang *et al.*, "Topology optimization with multiple materials via moving morphable component (MMC) method," *Int. J. Numer. Methods Eng.*, vol. 113, no. 11, pp. 1653–1675, 2018.

[54] W. Zhang, D. Li, J. Zhou, Z. Du, B. Li, and X. Guo, "A moving morphable void (MMV)-based explicit approach for topology optimization considering stress constraints," *Comput. Methods Appl. Mech. Eng.*, vol. 334, pp. 381–413, Jun. 2018.

[55] E. Somersalo, M. Cheney, and D. Isaacson, "Existence and uniqueness for electrode models for electric current computed tomography," *SIAM J. Appl. Math.*, vol. 52, no. 4, pp. 1023–1040, Jul. 1992.

[56] P. J. Vauhkonen, M. Vauhkonen, T. Savolainen, and J. P. Kaipio, "Three-dimensional electrical impedance tomography based on the complete electrode model," *IEEE Trans. Biomed. Eng*, vol. 46, no. 9, pp. 1150–1160, Sep. 1999.

[57] J. Kourunen, T. Savolainen, A. Lehikoinen, M. Vauhkonen, and L. M. Heikkinen, "Suitability of a PXI platform for an electrical impedance tomography system," *Meas. Sci. Technol.*, vol. 20, no. 1, 2009, Art. no. 015503.

[58] G. González, J. M. J. Huttunen, V. Kolehmainen, A. Seppänen, and M. Vauhkonen, "Experimental evaluation of 3D electrical impedance tomography with total variation prior," *Inverse Problems Sci. Eng.*, vol. 24, no. 8, pp. 1411–1431, 2016.

[59] M. Benning and M. Burger, "Modern regularization methods for inverse problems," *Acta Numerica*, vol. 27, pp. 1–111, May 2018.

[60] A. Nissinen, V. P. Kolehmainen, and J. P. Kaipio, "Compensation of modelling errors due to unknown domain boundary in electrical impedance tomography," *IEEE Trans. Med. Imag.*, vol. 30, no. 2, pp. 231–242, Feb. 2011.

[61] A. Lipponen, A. Seppänen, and J. P. Kaipio, "Electrical impedance tomography imaging with reduced-order model based on proper orthogonal decomposition," *J. Electron. Imag.*, vol. 22, no. 2, 2013, Art. no. 023008.

[62] B. Harrach and J. K. Seo, "Exact shape-reconstruction by one-step linearization in electrical impedance tomography," *SIAM J. Math. Anal.*, vol. 42, no. 4, pp. 1505–1518, 2010.